

Diffraction-limited plenoptic imaging with correlated light

Francesco V. Pepe,^{1,2,*} Francesco Di Lena,^{3,2} Aldo Mazzilli,³ Augusto Garuccio,^{3,2,4} Giuliano Scarcelli,⁵ and Milena D'Angelo^{3,2,4,†}

¹*Museo Storico della Fisica e Centro Studi e Ricerche “Enrico Fermi”, I-00184 Roma, Italy*

²*INFN, Sezione di Bari, I-70126 Bari, Italy*

³*Dipartimento Interateneo di Fisica, Università degli studi di Bari, I-70126 Bari, Italy*

⁴*Istituto Nazionale di Ottica (INO-CNR), I-50125 Firenze, Italy*

⁵*Fischell Department of Bioengineering, University of Maryland, College Park MD 20742 USA*

Traditional optical imaging faces an unavoidable trade-off between resolution and depth of field (DOF). To increase resolution, high numerical apertures (NA) are needed, but the associated large angular uncertainty results in a limited range of depths that can be put in sharp focus. Plenoptic imaging was introduced a few years ago to remedy this trade off. To this aim, plenoptic imaging reconstructs the path of light rays from the lens to the sensor. However, the improvement offered by standard plenoptic imaging is practical and not fundamental: the increased DOF leads to a proportional reduction of the resolution well above the diffraction limit imposed by the lens NA. In this paper, we demonstrate that correlation measurements enable pushing plenoptic imaging to its fundamental limits of both resolution and DOF. Namely, we experimentally demonstrate to maintain the imaging resolution at the diffraction limit while increasing the depth of field by a factor three. Our results represent the theoretical and experimental basis for the effective development of the promising applications of plenoptic imaging.

Plenoptic imaging (PI) is a novel optical method for recording visual information [1]. Its peculiarity is the ability to record both the position and the propagation direction of light in a single exposure. PI is currently employed in the most diverse applications, from stereoscopy [1–3], to microscopy [4–7], particle image velocimetry [8], particle tracking and sizing [9], wavefront sensing [10–13], as well as photography, where it currently enables digital cameras with refocusing capabilities [14, 15]. The capability of PI to simultaneously acquire multiple-perspective 2D images brings it among the fastest and most promising methods for 3D imaging with the available technologies [16]. In fact, high-speed and large-scale 3D functional imaging of neuronal activity has been demonstrated [7]. Furthermore, first studies for surgical robotics [17], endoscopic application [18] and blood-flow visualization [19] have been performed.

The key component of standard plenoptic cameras is a microlens array inserted in the native image plane, that reproduces repeated images of the main camera lens on the sensor behind it [1, 15]. This enables reconstruction of light paths, employed, in post-processing, for refocusing different planes, changing point of view and extending depth of field (DOF) within the acquired image. However, a fundamental tradeoff between spatial and angular resolution is naturally built in standard plenoptic imaging. If N_{tot} is the total number of pixels per line on the sensor, N_x the number of microlenses per line, and N_u the number of pixels per line associated with each microlens, then $N_x N_u = N_{\text{tot}}$. Essentially, standard PI gives the same resolution and DOF one would obtain with a N_u times smaller NA. The final advantage is thus practical

rather than fundamental, and is limited to higher luminosity (hence SNR) of the final image and parallel acquisition of multi-perspective images.

Correlation plenoptic imaging (CPI) has recently been proposed for overcoming this fundamental limit [20]. The main idea is to exploit the second-order spatio-temporal correlation properties of light to perform spatial and angular detection on two distinct sensors: Using correlated beams [20–22], high-resolution “ghost” imaging is performed on one sensor [23–27] while simultaneously obtaining the angular information on the second sensor. As a result, the relation between the spatial (N_x) and the angular (N_u) pixels per line, at fixed N_{tot} , becomes linear: $N_x + N_u = N_{\text{tot}}$ [20].

In this paper, we present the first experimental realization of CPI. We demonstrate that CPI has higher DOF and higher resolution than traditional PI; compared to conventional imaging, CPI maintains diffraction-limited resolution but triples DOF. Therefore, CPI truly pushes imaging to the fundamental limits imposed by the wave nature of light. Our results dramatically enhance the potentials of PI, paving the way towards its promising applications, especially in situations where high resolution and fast acquisition are required, such as microscopy and 3D imaging. In fact, compared to other 3D imaging techniques, CPI has the advantage of not requiring neither time-consuming scanning methods (as in confocal microscopy), nor delicate interferometric techniques (as in holography and ptychography), or fast pulsed illumination (as in time-of-flight imaging) [9, 28–30].

The experimental setup is reported in Figure 1 [?]. Based on the ghost imaging phenomenon [26, 27], intensity correlation measurement between each pixel of S_a and the whole sensor S_b enables retrieving an image of the object on the plane of S_a . Such “ghost” image is focused provided the distance z_a between the source and the sen-

* francesco.pepe@ba.infn.it

† milena.dangelo@uniba.it

source S_a is equal to the distance z_b between the source and the object [26, 27]: Due to the spatio-temporal correlation properties of chaotic light, the light source plays the role of focusing element, and replaces the lens of a standard imaging system characterized by image magnification $m = 1$ [27]. This justifies the name of *spatial sensor* for detector S_a , despite it detects a light beam that has never passed through the object. Like standard imaging, both maximum achievable resolution set by the diffraction-limit (Δx^f) and DOF of the ghost image are defined by the NA of the focusing element (here, chaotic light source), as seen from the object. In our case, $\Delta x^f = \lambda/\text{NA} = 120 \mu\text{m}$ and, for objects at the resolution limit, $\text{DOF} = \lambda/\text{NA}^2 = 14.7 \text{ mm}$. In our experiment, the pixel size has been chosen to match maximum achievable resolution: $\delta x = 50 \mu\text{m} \leq \Delta x^f/2$, thus enabling imaging at diffraction limit.

To understand how CPI enables increasing DOF of the acquired image and changing the viewpoint, let us study the role of high-resolution sensor S_b . Each pixel of this sensor corresponds to the source point from which the detected signal has been emitted. Correlation measurements between pixels of S_a and S_b may thus enable tracing “light rays” by joining each object point with each source point [20, 21]. Therefore, the high resolution of S_b does not inhibit retrieval of the (ghost) image of the object on S_a ; as shown in Eq. (8) of Supplemental Material, it simply makes it a coherent image. The conventional (incoherent) ghost image can be recovered by summing the correlations over the whole sensor S_b , which corresponds to using the typical “bucket” detector of ghost imaging.

Together with the numerical aperture NA_L of the lens L , the resolution of the source image retrieved by S_b is defined by the diffraction of light at the object, as discussed in section I of the Supplemental Material. In our experiment, the resolution limit defined by the lens ($\lambda/\text{NA}_L = 16 \mu\text{m}$) is smaller than the pixel size of S_b ($\delta u = \delta x = 50 \mu\text{m}$). Thus, the resolution on the source plane is defined either by diffraction at the object or by the pixel size, namely, $\Delta u = \max[\lambda z_b/a, 2\delta u/M]$, where a is the length scale of the smallest details of the object, and M is the magnification produced by the lens.

In our experiment, we have employed double-slit objects, to mimic small details and easily monitor the image resolution, both in the out-of-focus and in the refocused image. In Figure 2(a)-(b), we report the experimental results obtained for a double-slit mask with center-to-center distance $d = 0.40 \text{ mm} \lesssim 4 \Delta x^f$ and slit width $a = d/2$. In the left column, we report the focused (ghost) image retrieved on S_a by measuring correlation with the whole detector S_b , when $z_b = z_a$; this is analogous to the conventional image retrieved by any imaging system characterized by the given NA. In the central column, we show the out-of-focus images obtained when the mask is moved out of the focused plane, either closer [Figure 2(a)] or farther away [Figure 2(b)] from the source; again, this is equivalent to the conventional

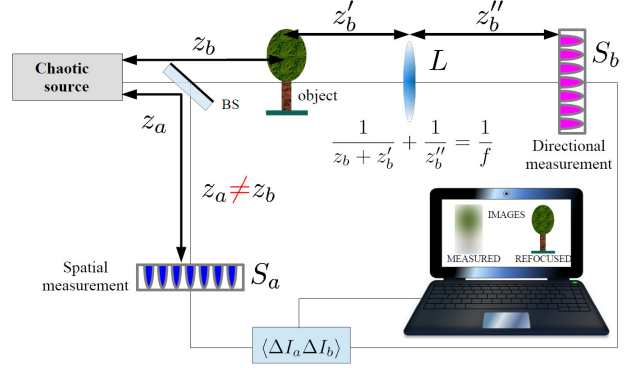


FIG. 1. Schematic representation of the experimental setup employed for correlation plenoptic imaging. The lens L replaces the whole microlens array of standard PI.

out-of-focus image retrieved by any imaging system with the given NA, when the object is moved closer or farther away from the focusing element. In the right column, we report the correlation plenoptic images obtained by refocusing the corresponding out-of-focus images of the central column. The CPI refocusing algorithm, similar to standard plenoptic imaging [15], takes the form [20]

$$\Sigma_{z_a, z_b}^{\text{ref}}(\rho_a) := \int d^2 \rho_b \Gamma_{z_a, z_b} \left(\frac{z_a}{z_b} \rho_a - \frac{\rho_b}{M} \left(1 - \frac{z_a}{z_b} \right), \rho_b \right), \quad (1)$$

where $\Gamma_{z_a, z_b}(\rho_a, \rho_b)$ represents the measured correlation of intensity fluctuations $\langle \Delta I_a \Delta I_b \rangle$ between point ρ_a on S_a and point ρ_b on S_b . In Figure 2(c), we show the results obtained with a larger object, having $d = 1.12 \text{ mm} \simeq 9 \Delta x^f$ and $a = d/2$, placed even farther away from the source. The refocusing power of CPI is here more apparent than in case (b), where the out-of-focus image could still be partially recognized; as expected, for object distances $z_b > z_a$, the maximum achievable DOF of CPI is constraint by diffraction at the object. Both the refocusing capability of CPI, and the excellent agreement between experimental data (points) and theoretical prediction (solid line) are apparent in Figure 2. [?]

To understand the physical origin of the refocusing capability of CPI, we report in Figure 3(a) the raw data obtained by measuring the pixel-by-pixel correlation of intensity fluctuations between S_a and S_b [i.e., $\Gamma_{z_a, z_b}(\rho_a, \rho_b)$]. For each pixel of the angular sensor S_b , we observe on S_a a displaced image of the object: Hence, imaging the light source on the high-resolution sensor S_b enables changing the perspective on the observed scene [?]. This result explains why the standard ghost image reported in Figure 3(c) is blurred: When no angular information is retrieved (i.e., when integration over S_b is performed), all displaced images overlap giving rise to the out-of-focus image $\Sigma_{z_a, z_b}(\rho_a) = \int d^2 \rho_b \Gamma_{z_a, z_b}(\rho_a, \rho_b)$. In ghost imaging, the integration performed by the bucket detector clearly erases the precious information contained in the raw data of CPI. On the contrary, CPI exploits the

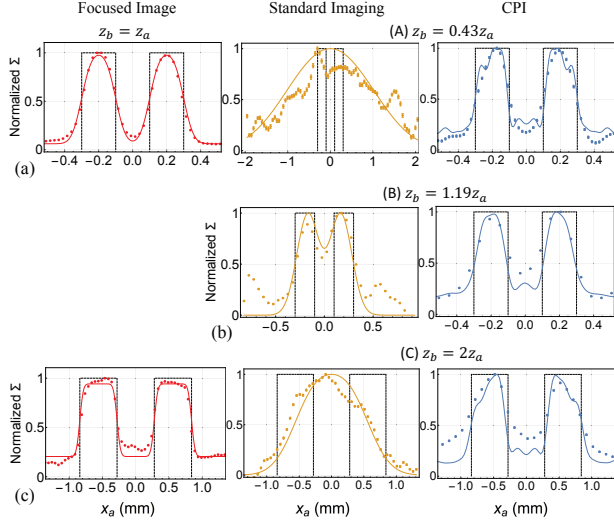


FIG. 2. Comparison between the focused images obtained at $z_b = z_a$ (left column), the out-of-focus images obtained after moving the object in $z_b \neq z_a$ (central column), and the CPI refocused images (right column), as obtained in the setup of Figure 1, in three experimental scenarios, denoted as measurement A, B and C, respectively. Points indicate experimental data, taken with a pixel size at the diffraction limit ($\delta x = 50 \mu\text{m}$). The continuous curve is the theoretical prediction, as reported in Section IV of the Supplemental Material, and the dashed line is the object mask. In the refocused images, the pixel size is scaled by a factor z_b/z_a , in line with Eq. (1) (see also Eq. (12) of the Supplemental Material).

extra information gained by the high resolution detector S_b . As shown in Figure 3(b), all displaced images are realigned by the reshaping and resizing algorithm that appears in the integrand of Eq. (1), hence, no blurring occurs anymore upon integration over S_b , and the refocused image of Figure 3(d) is obtained [?].

Let us now focus our attention on the central point of the paper, namely, the unique opportunity offered by CPI to refocus without sacrificing diffraction-limited image resolution defined by numerical aperture of the imaging system. In Figure 4(c), the dashed (white) line represents the geometrical-optics prediction for “perfect” refocusing in CPI, which is given by the relation [20]

$$\left| 1 - \frac{z_a}{z_b} \right| < \frac{\Delta x}{\Delta u} = \frac{dz_a/z_b}{\max[\lambda z_b/a, 2\delta_u/M]} \quad (2)$$

with Δx the resolution on sensor S_a , and Δu the resolution on source plane. In the right hand side of Eq. (2), we have expressed both quantities in the simple case of a double-slit object of width a and center-to-center distance $d = 2a$: The resolution Δx is defined by the geometrical projection of the image of the double slit on the sensor plane; the resolution Δu is generally defined by diffraction at the object (i.e., $\Delta u = \lambda z_b/a$), but the pixel size δ_u enters into play for objects extremely close to the light source (i.e., for $z_b = 2\delta_u a/(M\lambda)$). The physical quantities defining spatial and angular resolution of CPI

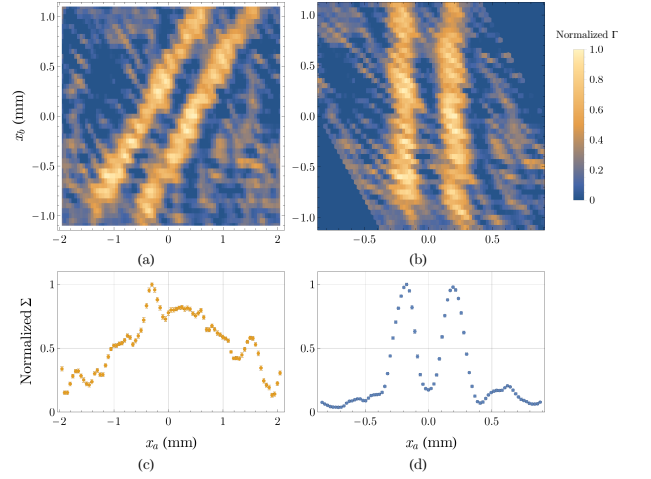


FIG. 3. (a) Experimental results obtained by measuring the pixel-by-pixel correlation between S_a and S_b , in the exact same scenario reported in Figure 2(a). (b) Result of the refocusing algorithm reported in the integrand of Eq. (1), as applied to the raw data of panel (a). (c) and (d): Results of the integration over the angular sensor S_b of the data of panel (a) and (b), respectively. The first one coincides with the standard ghost image, the second one represents the final refocused image of CPI, as described by Eq. (1).

are thus the object position z_b and the object features a and d . The density plot in Figure 4(c) reports visibility $V(d/\Delta x^f, z_b - z_a)$ of the refocused CPI images of double-slit masks, evaluated in the present experimental setup from the theoretical predictions reported in Section V of Supplemental Material. Besides giving the degree of reliability of the geometrical prediction of Eq. (2), this plot unveils the physical limit of resolution and DOF in CPI [?].

To compare CPI with both standard imaging and standard PI, we consider imaging devices having the same NA as the light source in our experiment, and report in Figures 4(a) and (b) the visibility they achieve [?]. For standard PI, we have considered $N_u = 3$ to avoid strongly compromising the image resolution. Comparison of Figures 4(a), (b) and (c) indicates that CPI combines at best the advantages of standard imaging and plenoptic imaging: It preserves the resolution of standard imaging while increasing the DOF even beyond the typical values of standard PI. Interestingly, for close up ($z_b < z_a$), object details larger than $d \gtrsim \sqrt{8\lambda z_a} \simeq 2.8\Delta x^f$ (i.e., the refocusing limit corresponding to $z_b = z_a/2$) can always be refocused by CPI, no matter how close the object is to the source. For $z_b > z_a$, the maximum achievable depth of field is significantly larger than in both standard imaging and standard PI. As demonstrated in Section V of the Supplemental Material (see Figures 2 and 3 therein), the refocusing range in CPI is only limited by interference at the object, for close-up, and by diffraction at the object, for distant objects. Hence, CPI reaches the fundamental limits imposed by wave nature of light to both image resolution and DOF.

From Figure 4, one can infer that the double-slits associated with experimental points A, B and C can only be refocused by CPI. In particular, the object corresponding to the experimental points A and B can be refocused by CPI in a range three times larger than in standard imaging, and twice larger than in a standard PI device with a three times worst spatial resolution. The wider double-slit corresponding to the point C has twice the DOF of standard imaging, and a slightly wider DOF than in standard PI with $N_u = 3$. Interestingly, the DOF of the standard ghost image represents the CPI axial resolution: $\Delta z^{CPI} = \lambda/NA^2$. Hence, the ratio between depth of fields of CPI and standard imaging fixes the number of planes that can be refocused by CPI.

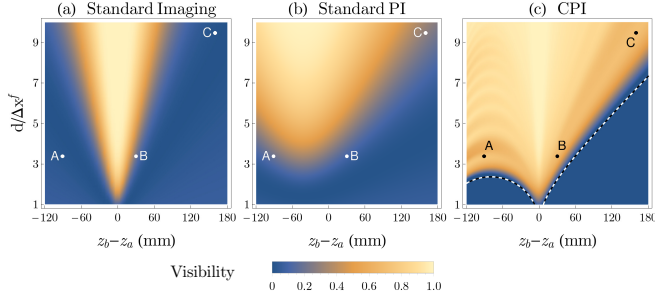


FIG. 4. Analysis of the range of perfect refocusing for double-slit objects with $d = 2a$; the slit distance d is normalized to the resolution of the focused image Δx^f . Visibility is computed by considering (a) standard imaging, (b) standard plenoptic imaging (with $N_u = 3$), and (c) CPI devices sharing the same NA employed in the experiment. Points A, B and C correspond to the experimentally analyzed cases (see Figure 2), while the (white) dashed line in panel (c) is the geometrical perfect refocusing limit as given by Eq. (2).

To summarize the above results, in Figure 5, we plot the DOF enhancement offered by CPI with respect to standard PI as a function of the resolution compromise of conventional PI (namely, the number of angular pixels N_u of standard PI, which corresponds to the ratio between the maximum image resolutions of standard PI and standard imaging/CPI); the DOF enhancement is defined as the ratio between the maximum achievable DOF of CPI and standard PI. All parameters are the same employed in Figure 4. To better emphasize the lack of refocusing limit for close up, we have chosen to separately plot the two cases of object closer to and farther from the conjugate plane $z_b = z_a$. CPI is seen to significantly overcome the DOF of both standard imaging (corresponding to $N_u = 1$) and standard plenoptic imaging, while maintaining the diffraction limited resolution of standard imaging. In line with the results in Figure 4, the DOF of standard PI and CPI are equal only for $z_b < z_a$, when large enough objects are considered; in all other cases, CPI outperforms conventional PI.

Conclusions and outlook. — We have demonstrated the ability of CPI to push plenoptic imaging to its fundamental limits of both resolution and maximum achievable

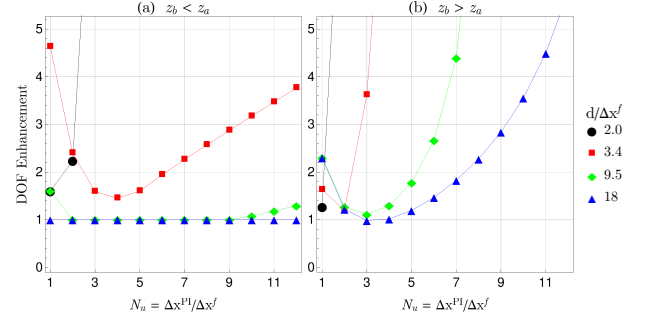


FIG. 5. Comparison between standard PI and CPI in terms of maximum achievable DOF versus resolution. The comparison is made for double slits of varying distance d , and width $a = d/2$. DOFs are evaluated by considering the maximum (z_b^M) and the minimum (z_b^m) values of the object distance for which the image is still resolved based on Rayleigh criterion (namely, $V \geq 10\%$). We report the results for (a) $z_b < z_a$, and (b) $z_b > z_a$ obtained by considering the experimental setup for CPI, and an equivalent standard PI device.

DOF: Different from standard PI, CPI has no constraints on the image resolution, which stays diffraction-limited as in standard imaging systems. Still, CPI enables increasing the depth of field well beyond the typical DOF of standard imaging. The advantages of both standard and plenoptic imaging are thus combined at best in CPI, whose maximum achievable DOF is solely limited by interference and diffraction at the object (see, e.g., Figures 2 and 3 of the Supplemental Material). Importantly, plenoptic imaging is the first application in which the surprising properties of correlated systems are effectively used to beat intrinsic limits of standard imaging systems.

CPI has the potential to strongly improve the performances of both microscopy, where high lateral and axial resolutions are required together with large DOF, and 3D imaging, where fast multiperspective acquisitions are desired. Future studies will be devoted to acquisition time optimization, considering hardware (fast CMOS, smart sensors [31]) and software solutions (compressed-sensing and sparse measurement techniques [32]) to regain the single-shot advantage of conventional plenoptic imaging.

ACKNOWLEDGMENTS

The Authors thank C. Plantamura and C. Bevilacqua for developing the LabVIEW program employed in the experiment, and T. Macchia for participating at the preliminary experimental activity. MD acknowledges financial support from the Italian Ministry of Education, University and Research (MIUR), projects PONa3_00369 (“Laboratorio per lo Sviluppo Integrato delle Scienze e delle Tecnologie dei Materiali Avanzati e per dispositivi innovativi -LABORATORIO SISTEMA”). MD, FD, AM and AG acknowledge financial support from MIUR, project n. PON02-00576-3333585 (P.O.N. RICERCA E

COMPETITIVITÀ 2007-2013 - Avviso n. 713/Ric. del 29/10/2010, Titolo II - “Sviluppo/Potenziamento di DAT e di LPP”). MD, FD, AG and FVP are partially supported by Istituto Nazionale di Fisica Nucleare (INFN) through the projects “QUANTUM” and “PICS”.

Appendix A: CPI with chaotic light

Let us review the main steps for demonstrating the refocusing capability of CPI, and Eq. (1); a complete discussion can be found in Refs. [20, 21]. Thank to the chaotic nature of our light source, the intensities measured at point ρ_a of the sensor S_a at time t_a and at point ρ_b of the sensor S_b at time t_b are characterized by spatio-temporal correlations, described by the Glauber correlation function [33]

$$G^{(2)}(\rho_a, \rho_b; t_a, t_b) = \left\langle E_a^{(-)}(\rho_a, t_a) E_b^{(-)}(\rho_b, t_b) E_b^{(+)}(\rho_b, t_b) E_a^{(+)}(\rho_a, t_a) \right\rangle. \quad (\text{A1})$$

Here, $E_i^{(\pm)}$ are the positive- and negative-frequency components of the electric field [$E^{(+)} = (E^{(-)})^\dagger$] at each detector, and the expectation value is evaluated by considering the quantum state ρ of the source. The fields are propagated from the output plane of the source to each detector by the paraxial optical transfer functions g_a and g_b , as

$$E_i^{(+)}(\rho_i, t_i) = \int d\Omega \int d^2\kappa a_{\mathbf{k}} e^{-i\Omega t_i} g_i(\rho_i, \mathbf{k}), \quad (\text{A2})$$

where the integral runs over frequencies Ω and transverse momenta κ , and $a_{\mathbf{k}}$ is the canonical field operator of the mode \mathbf{k} . In the paraxial approximation, the 3D wave vector reads $\mathbf{k} = (\kappa, \Omega/c)$. When the source is both stationary and quasi-monochromatic, with peak frequency ω , the correlation function depends only on $\tau = t_a - t_b$, and the time dependent part approximately factorizes with respect to the space-dependent part. In addition, for a chaotic source, the four-point expectation value involved in Eq. (A1) reduces to the sum of two terms,

$$\langle a_{\mathbf{k}_1}^\dagger a_{\mathbf{k}_2}^\dagger a_{\mathbf{k}_3} a_{\mathbf{k}_4} \rangle \propto \delta(\mathbf{k}_1 - \mathbf{k}_4) \delta(\mathbf{k}_2 - \mathbf{k}_3) + \delta(\mathbf{k}_1 - \mathbf{k}_3) \delta(\mathbf{k}_2 - \mathbf{k}_4). \quad (\text{A3})$$

Therefore, upon neglecting the time dependence (i.e., working within the coherence time of the source), the second-order correlation function in Eq. (A1) reads

$$G^{(2)}(\rho_a, \rho_b) = I_a(\rho_a) I_b(\rho_b) + \Gamma(\rho_a, \rho_b), \quad (\text{A4})$$

where the first term is the mere product of intensities at the points ρ_i on S_i , with $i = a, b$. The second term

$$\Gamma(\rho_a, \rho_b) = \left| \int d^2\kappa g_a^*(\rho_a, \kappa) g_b(\rho_b, \kappa) \right|^2 \quad (\text{A5})$$

represents the nontrivial part of the second-order correlation, that yields the correlation of intensity fluctuations and encodes plenoptic imaging properties.

To unveil such properties, we first need to compute the transfer functions in the setup of Figure 1. Up to irrelevant normalization factors and phases, we have:

$$g_a(\rho_a, \kappa) = \int d^2\rho_s f(\rho_s) e^{i(\kappa - \frac{\omega}{cz_a} \rho_a) \cdot \rho_s} G(\rho_s) \Big|_{\frac{\omega}{cz_a}} \quad (\text{A6})$$

in the reflected arm and

$$g_b(\rho_b, \kappa) = \int d^2\rho_s \int d^2\rho_o f(\rho_s) A(\rho_o) \times G(\rho_s) \Big|_{\frac{\omega}{cz_b}} e^{i\kappa \cdot \rho_s - \frac{i\omega}{cz_b} \rho_o \cdot (\rho_s + \frac{\rho_b}{M})} \quad (\text{A7})$$

in the transmitted arm, with $G(\rho)_{[\beta]} = \exp(i\beta \rho^2/2)$, $A(\rho_o)$ the object transmission function, and $f(\rho_s)$ the source amplitude profile. Notice that in Eq. (A7) we have assumed that the lens L , that focuses the image of the source on the sensor S_b with magnification M , is diffraction-limited. Given the propagators of Eqs. (A6)-(A7), one can compute the nontrivial part of the correlation function in Eq. (A5), which yields, up to trivial factors,

$$\Gamma_{z_a, z_b}(\rho_a, \rho_b) = \left| \int d^2\rho_o \int d^2\rho_s A(\rho_o) F(\rho_s) \times G(\rho_s) \Big|_{\frac{\omega}{c}(\frac{1}{z_b} - \frac{1}{z_a})} e^{-\frac{i\omega}{cz_b}[(\rho_o - \frac{z_b}{z_a} \rho_a) \cdot \rho_s + \rho_o \cdot \frac{\rho_b}{M}]} \right|^2 \quad (\text{A8})$$

where $F = |f|^2$ is the source intensity profile.

On one hand, Eq. (A8) indicates that a focused *coherent image* of the object $A(\rho_o)$ is obtained when $z_a = z_b$. The focusing condition is shared by the ghost image, which is given by the integral of Eq. (A8) over the sensor S_b :

$$\Sigma_{z_a, z_b}(\rho_a) = \int d^2\rho_b \Gamma_{z_a, z_b}(\rho_a, \rho_b). \quad (\text{A9})$$

Interestingly, the focused ghost image

$$\Sigma_{z_a, z_a}(\rho_a) \propto \int d^2\rho_o |A(\rho_o)|^2 \left| \tilde{F} \left[\frac{\omega}{cz_a} (\rho_o - \rho_a) \right] \right|^2 \quad (\text{A10})$$

is formally identical to a standard *incoherent image* (with no magnification): It sets a quasi one-to-one correspondence between points of the object plane and points of the sensor S_a . The point-spread function (PSF) of the ghost image is given by the squared modulus of the Fourier Transform of the source intensity profile (\tilde{F}); in ghost imaging, the source intensity profile thus plays the exact same role that a lens plays in standard imaging. The image resolution $\Delta\rho_a \simeq 2\pi cz_a/(\omega D_s) =: \lambda/NA$ is defined by the numerical aperture NA of the focusing element (here, the source), characterized by the effective diameter D_s .

On the other hand, due to the first-order image of the source on sensor D_b , Eq. (A8) also entails a correspondence between points of the source plane and pixels of the sensor S_b ($\rho_b = -M\rho_s$), whose uncertainty $\Delta\rho_b = M\lambda z_b/a$ is determined by the typical size a of the smallest detail of the object, that acts as a pupil for the lens L , and by the distance z_b . The resolution of the source image is thus limited by diffraction at the object.

The plenoptic properties of $\Gamma_{(z_a, z_b)}$ clearly emerge in the geometrical optics limit $\omega \rightarrow \infty$. Indeed, in this limit, the double integral in Eq. (A8) can be approximated by a stationary-phase approximation, which reveals that the object and source points that provide the prominent contribution to the integral are related to the detection points by

$$\rho_s = -\frac{\rho_b}{M}, \quad (\text{A11})$$

$$\rho_o = \frac{z_b}{z_a}\rho_a - \frac{\rho_b}{M}\left(1 - \frac{z_b}{z_a}\right), \quad (\text{A12})$$

The first result is expected by the aforementioned first-order imaging of the source. The second line is nontrivial, since it is not related to any first-order imaging property, but it connects points of the object to points of *both* sensors. Thus, in the geometrical optics limit, we can deduce the asymptotic behavior of the nontrivial part of the second-order correlation function:

$$\Gamma_{z_a, z_b}(\rho_a, \rho_b) \sim F\left(-\frac{\rho_b}{M}\right)^2 \left| A\left[\frac{z_b}{z_a}\rho_a - \frac{\rho_b}{M}\left(1 - \frac{z_b}{z_a}\right)\right] \right|^2. \quad (\text{A13})$$

If $z_b \neq z_a$, the integration of this result over ρ_b , which is equivalent to retrieving an out-of-focus (incoherent) ghost image, erases information on the aperture function of the object, and leads to a blurred image. This indicates the crucial role played by the high-resolution detector S_b , as opposed to the bucket detector of standard ghost imaging. In fact, based on Eq. (A13), one can use the information obtained from intensity correlation measurements to *refocus* the coherent correlation plenoptic image of the object:

$$\Gamma_{z_a, z_b}\left[\frac{z_a}{z_b}\rho_a - \frac{\rho_b}{M}\left(1 - \frac{z_a}{z_b}\right), \rho_b\right] \sim F\left(-\frac{\rho_b}{M}\right)^2 |A(\rho_a)|^2. \quad (\text{A14})$$

The integration of the refocused correlation function of Eq. (A14) over ρ_b [as reported in Eq. (1)] increases the signal-to-noise ratio of the final refocused image obtained by CPI without blurring it, as demonstrated in Figure 3(d).

Appendix B: CPI with a Gaussian source

Based on Eq. (A8) of the main text, the correlation of intensity fluctuations can be expressed as the convolution of the aperture function of the object with the (coherent)

CPI point-spread function $\mathcal{C}(\rho)$, namely,

$$\Gamma_{z_a, z_b}(\rho_a, \rho_b) = \left| \int d^2\rho_o A(\rho_o) e^{-\frac{i\omega\rho_o \cdot \rho_b}{cz_b M}} \mathcal{C}\left(\rho_o - \frac{z_b}{z_a}\rho_a\right) \right|^2. \quad (\text{B1})$$

In the case of a source with Gaussian intensity profile $F(\rho_s) = \exp[-\rho_s^2/(2\sigma^2)]/(2\pi\sigma^2)$, the PSF of the correlation plenoptic image takes the simple form [21]

$$\mathcal{C}(\rho) \propto \exp\left(-\frac{1}{2}\left(\frac{\omega\sigma}{cz_b}\right)^2 \frac{|\rho|^2}{1 - \frac{i\omega\sigma^2}{cz_b}\left(1 - \frac{z_b}{z_a}\right)}\right). \quad (\text{B2})$$

It is also immediate to verify that the PSF \mathcal{J} of the (incoherent) ghost image is related to the PSF of CPI by the relationship $\mathcal{J}(\rho) \propto |\mathcal{C}(\rho)|^2$. In the case of a Gaussian source, we have [21]:

$$\mathcal{J}(\rho) \propto \exp\left(-\left(\frac{\omega\sigma}{cz_b}\right)^2 \frac{|\rho|^2}{1 + \left(\frac{\omega\sigma^2}{cz_b}\left(1 - \frac{z_b}{z_a}\right)\right)^2}\right). \quad (\text{B3})$$

Appendix C: Experimental methods

The experimental setup for demonstrating CPI is reported in Figure 1. The chaotic source is made by a single-mode laser diode with wavelength $\lambda = 980$ nm, $P = 300$ mW (Sheaumann M9-980-0300-D5P), impinging on a rotating ground glass disk, spinning at about 9 Hz, at a distance of about 2 cm from the center. The source coherence time is $\tau_{\text{coh}} \sim 10^{-4}$ s. Light from the source is divided by a symmetric beam-splitter (BS). The reflected beam propagates in free space toward the spatial sensor S_a , characterized by a pixel size of $50 \mu\text{m}$, and placed at a distance $z_a = 160$ mm from the source. The transmitted beam passes through the object of interest, propagates toward a lens (L) of focal length $f = 250$ mm, and reaches the angular sensor S_b , whose pixel size is also $50 \mu\text{m}$. The angular detector S_b is placed in the conjugate plane of the source, whose image is magnified by $M = 1.3$. Spatio-temporal correlation measurements are performed between the signals at the two sensors. The AC coupling of signals enables measuring correlation of intensity fluctuations $\langle \Delta I_a \Delta I_b \rangle$. The sensors are amplified photodiodes (Thorlabs PDA36A-EC) mounted on motorized translational stages (PI M-231.17 Linear Actuators); the output signals are AC coupled to an oscilloscope (Teledyne Lecroy HDO6104) that performs the required temporal correlation measurement. The gains of the two photodiodes are set to 60 dB. The results of the correlation measurement performed for each position of the two detectors are sent to a computer, where a LabVIEW program controls both the oscilloscope and the translational stages. The acquisition time is $\tau_{\text{meas}} = 1 \text{ s} \sim 10^4 \tau_{\text{coh}}$ for each correlation measurement. The acquisition time could have been shortened both

by reducing N to about 100, which still gives an acceptable $SNR > 50$, and by lowering the coherence time of the source, which we set to optimally match the response time of the detectors.

Appendix D: Model of the experimental source

In our experiment, the double-slit masks employed as objects are parallel to the y axis, hence, the relevant PSFs for coherent CPI and incoherent ghost imaging are the one-dimensional projections of Eqs (B2) and (B3), namely, $\mathcal{C}_1(x) = \int dy \mathcal{C}(x, y)$ and $\mathcal{J}_1(x) = \int dy \mathcal{J}(x, y)$. It is worth emphasizing that the incoherent one-dimensional PSF is generally not proportional to $|\mathcal{C}_1|^2$.

The intensity profile of the experimental chaotic source along x has been fitted by a Gaussian function with $\sigma = 0.89$ mm. This Gaussian approximation provides sensible predictions on the experimental correlation measurements as long as the object is well out-of-focus, namely, when the $(1 - z_b/z_a)$ -dependent parts are dominant in the denominators of Eqs. (B2)-(B3). However, when we experimentally retrieve the focused image (i.e., when $z_b = z_a$) of a point object, we obtain a PSF larger than expected; this is mostly due to the deviation of the source profile from the Gaussian form, to the effective multimode operation of the diode laser, as well as to the interplay between the x and y directions. These two regimes are interpolated by the expressions

$$\mathcal{C}_1(x) \propto \exp\left(-\frac{1}{2}\left(\frac{\omega\sigma}{cz_b}\right)^2 \frac{x^2}{K^2 - \frac{i\omega\sigma^2}{cz_b}(1 - z_b/z_a)}\right), \quad (\text{D1})$$

$$\mathcal{J}_1(x) \propto \exp\left(-\left(\frac{\omega\sigma}{cz_b}\right)^2 \frac{x^2}{K^2 + \left(\frac{\omega\sigma^2}{cz_b}(1 - z_b/z_a)\right)^2}\right), \quad (\text{D2})$$

which yield the best fit to the experimentally measured PSFs at $z_b = z_a$ for $K = 2.1$.

The result in Eq. (D2), typical of both ghost imaging and conventional incoherent imaging [?], also enables a clearer understanding of Figure 4, where the visibility of the incoherent image is seen to be asymmetric with respect to the object position $z_b = z_a$. In fact, when z_a is kept fixed as in our experimental case, the image of a one-dimensional object placed in x_o at a distance $z_b \neq z_a$ from the source is a Gaussian centered in $x_a = x_o/\alpha$, with $\alpha = z_b/z_a$, and characterized by the width

$$\frac{\sigma_i(\alpha)}{\alpha} = \frac{1}{\alpha} \sqrt{\frac{1}{2}\left(K\frac{cz_a}{\omega\sigma}\right)^2 \alpha^2 + \frac{\sigma^2}{2}(1 - \alpha)^2}. \quad (\text{D3})$$

The factor $1/\alpha$ is a magnification due to the geometrical projection of the object onto a plane different from its conjugate image plane. Hence, the quantity in Eq. (D3)

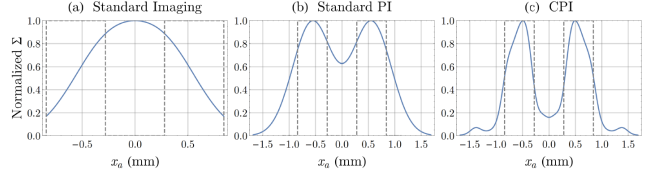


FIG. 6. Theoretical comparison between: (a) standard imaging, (b) standard plenoptic imaging (with $N_u = 3$), and (c) CPI, for a double-slit mask with $a = 0.56$ mm and $d = 2a$ placed in $z_b = 2z_a = 320$ mm, as given by imaging systems sharing the same NA as our setup (see Figure 1).

that actually determines the image resolution is $\sigma_i(\alpha)$, and is minimized by

$$\bar{\alpha} = \left(1 + \left(K\frac{cz_a}{\omega\sigma^2}\right)^2\right)^{-1}. \quad (\text{D4})$$

The quantity $\bar{\alpha}$ is generally smaller than one, and the difference from unity is larger for smaller source widths; in fact, the asymmetry can be appreciated only in panel (b) of Figure 4. The asymmetry would disappear if one fixes the object distance z_b and varies the sensor distance z_a .

Appendix E: DOF advantage of CPI

In Fig. 6, we report the comparison of CPI with both conventional imaging and conventional PI: Beside gaining diffraction limited resolution, CPI clearly enables improving the DOF with respect to both conventional modalities. We have chosen to work in the same scenario corresponding to the experimental measurement (C) reported in Figure 2(c), since the predictions associated with both measurements (A) and (B) give better results, namely, a larger improvement of CPI with respect to the two conventional modalities.

To better understand the origin of this result, we shall compare the DOF of CPI and ghost imaging (which is always representative of standard imaging). In Figures 7 and 8, we report the incoherent ghost image (left column)

$$\Sigma_{z_a, z_b}\left(\frac{z_a}{z_b}x_a\right) = \int dx_o |A(x_o)|^2 \mathcal{J}_1(x_o - x_a), \quad (\text{E1})$$

the coherent image from CPI (central column)

$$\Gamma_{z_a, z_b}\left(\frac{z_a}{z_b}x_a, x_b = 0\right) = \left|\int dx_o A(x_o) \mathcal{C}_1(x_o - x_a)\right|^2, \quad (\text{E2})$$

and the refocused image from CPI (right column)

$$\Sigma_{z_a, z_b}^{\text{ref}}(x_a) = \int dx_b \Gamma_{z_a, z_b}\left(\frac{z_a}{z_b}x_a - \frac{x_b}{M}\left(1 - \frac{z_a}{z_b}\right), x_b\right), \quad (\text{E3})$$

for three single-slit masks of different width a , and for a double-slit mask. The results have been obtained by

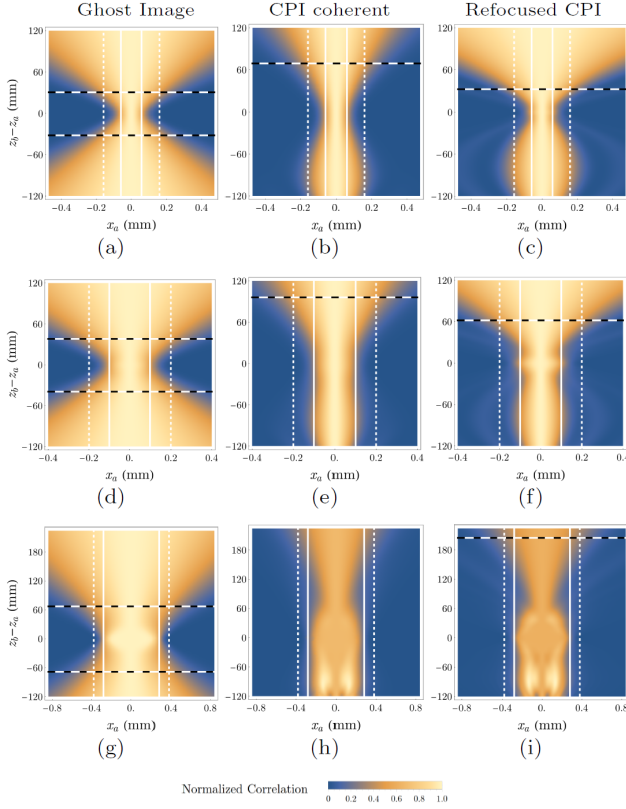


FIG. 7. Comparison between the incoherent ghost images [panels (a), (d), (g)], the coherent images from CPI [(b), (e), (h)], and the refocused image from CPI [(c), (f), (i)], for three different single-slit masks of width $a = 120 \mu\text{m} = \Delta x^f$ (top panels), $a = 200 \mu\text{m} = 1.7 \Delta x^f$ (central panels), and $a = 560 \mu\text{m} = 4.7 \Delta x^f$. The density plots report the correlation functions of Eq. (E1)–(E3), normalized to their value in $x_a = 0$, for any value of $z_b - z_a$, evaluated in the setup of Figure 1. The solid (white) lines represent the size of the object, while the (white) dashed lines represent the tolerance on the blurring of the images, which is, the resolution limit. The (black) dotted lines indicate the DOF.

considering the experimental setup of Figure 1, with a Gaussian source of width $\sigma = 0.89 \text{ mm}$, as retrieved from the fit of the source intensity profile. In line with the experiment, we fix z_a while changing z_b . In Figure 7, the resolution limit (vertical dashed lines) is defined by adding to the half width $a/2$ of the object the quantity $2\sqrt{2} \ln 2 \sigma_{PSF}$ corresponding to the Rayleigh criterion for a Gaussian PSF of width σ_{PSF} [?]; the DOF (horizontal dashed lines) is given by the value of $z_b - z_a$ at which the half width at half maximum of the image reaches the resolution limit. In Figure 8, the DOF is obtained by the visibility of the double-slit image: The Rayleigh

resolution criterion applied to the image of a double-slit having slit width a and center-to-center distance $d = 2a$, gives a visibility $V = 10\%$. Based on both Figures 7-8, the coherent image always has a wider DOF than ghost imaging; this results in the enhanced refocusing range of

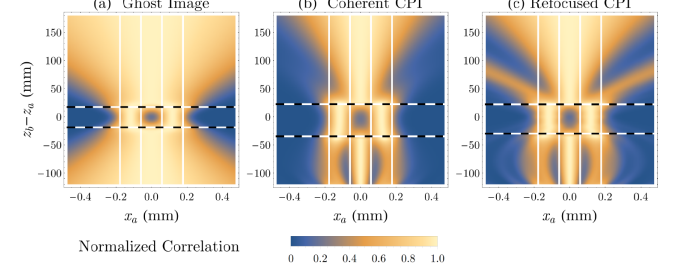


FIG. 8. Comparison between: (a) the incoherent ghost image, (b) the coherent image from CPI, and (c) the refocused image from CPI, for a double-slit mask of width $a = 120 \mu\text{m} = \Delta x^f$ and slit separation $d = 2a$. The density plots report the correlation functions of Eq. (22), (23), and (24), normalized to their value in $x_a = 0$, for any value of $z_b - z_a$, evaluated in the setup of Figure 1. The solid (white) lines represent the size of the object. The (black) dotted lines indicate the DOF, defined as the value of $z_b - z_a$ where the visibility drops below 10% (see text for details).

CPI. But what limits the maximum achievable DOF of the refocused correlation plenoptic image?

On one hand, for close objects ($z_b < z_a$), Figure 7 predicts an unlimited DOF for the coherent image, which results in an unlimited refocusing capability for CPI. However, due to the coherent nature of CPI, a complete analysis of the DOF requires accounting for interference: Based on Figure 8, interference between light passing through the two slits limits the DOF associated with close objects, both for the coherent and for the final refocused image from CPI.

On the other hand, for far objects, the final refocused image does not necessarily maintain the improved DOF of its underlying coherent images. This is due to the detrimental effect diffraction has on the reliability of the retrieved angular information: The one-to-one correspondence between points of the angular sensor S_b and points on the source plane may be compromised by diffraction at the object. Notice that for large enough objects, diffraction enters into play only at object distances $z_b > z_a$ that fall outside the DOF of the coherent image; hence, the refocused image has essentially the same DOF of its underlying coherent images.

In summary, CPI enables imaging object details at the resolution limit, as well as improving the DOF with respect to standard imaging; the improvement grows with increasing object size, and is only limited by diffraction.

- [2] S. Muenzel and J. W. Fleischer, "Enhancing layered 3d displays with a lens," *Applied Optics* **52**, D97 (2013).
- [3] M. Levoy and P. Hanrahan, "Light field rendering," in *Proceedings of the 23rd annual conference on Computer graphics and interactive techniques*, pp. 31–42, ACM (1996).
- [4] M. Levoy, R. Ng, A. Adams, M. Footer, and M. Horowitz, "Light field microscopy," *ACM Transactions on Graphics (TOG)* **25**, 924 (2006).
- [5] M. Broxton, L. Grosenick, S. Yang, N. Cohen, A. Andelman, K. Deisseroth, and M. Levoy, "Wave optics theory and 3-d deconvolution for the light field microscope," *Optics Express* **21**, 25418 (2013).
- [6] W. Glastre, O. Hugon, O. Jacquin, H. G. de Chatellus, and E. Lacot, "Demonstration of a plenoptic microscope based on laser optical feedback imaging," *Optics Express* **21**, 7294 (2013).
- [7] R. Prevedel, Y.-G. Yoon, M. Hoffmann, N. Pak, G. Wetzstein, S. Kato, T. Schrödel, R. Raskar, M. Zimmer, E. S. Boyden, and A. Vaziri, "Simultaneous whole-animal 3d imaging of neuronal activity using light-field microscopy," *Nature Methods* **11**, 727 (2014).
- [8] T. W. Fahringer, K. P. Lynch, and B. S. Thurow, "Volumetric particle image velocimetry with a single plenoptic camera," *Measurement Science and Technology* **26**, 115201 (2015).
- [9] E. M. Hall, B. S. Thurow, and D. R. Guildenbecher, "Comparison of three-dimensional particle tracking and sizing using plenoptic imaging and digital in-line holography," *Applied Optics* **55**, 6410 (2016).
- [10] C. W. Wu, *The plenoptic sensor*, PhD thesis, 2016.
- [11] Y. Lv, R. Wang, H. Ma, X. Zhang, Y. Ning, and X. Xu, "SU-G-IeP4-09: Method of human eye aberration measurement using plenoptic camera over large field of view," *Medical Physics* **43**, 3679 (2016).
- [12] C. Wu, J. Ko, and C. C. Davis, "Using a plenoptic sensor to reconstruct vortex phase structures," *Optics Letters* **41**, 3169 (2016).
- [13] C. Wu, J. Ko, and C. C. Davis, "Imaging through strong turbulence with a light field approach," *Optics Express* **24**, 11975 (2016).
- [14] <https://www.lytro.com/illum>, <http://www.raytrix.de/>.
- [15] R. Ng, M. Levoy, M. Brédif, G. Duval, M. Horowitz, and P. Hanrahan, "Light field photography with a hand-held plenoptic camera," *Computer Science Technical Report CSTR* **2**, 1 (2005).
- [16] X. Xiao, B. Javidi, M. Martinez-Corral, and A. Stern, "Advances in three-dimensional integral imaging: sensing, display, and applications," *Applied Optics* **52**, 546 (2013).
- [17] A. Shademan, R. S. Decker, J. Opfermann, S. Leonard, P. C. Kim, and A. Krieger, "Plenoptic cameras in surgical robotics: Calibration, registration, and evaluation," in *2016 IEEE International Conference on Robotics and Automation (ICRA)*, pp. 708–714, IEEE (2016).
- [18] H. N. Le, R. Decker, J. Opferman, P. Kim, A. Krieger, and J. U. Kang, "3-d endoscopic imaging using plenoptic camera," in *CLEO: Applications and Technology*, paper AW4O.2, Optical Society of America (2016).
- [19] M. F. Carlsohn, A. Kemmling, A. Petersen, and L. Wietzke, "3d real-time visualization of blood flow in cerebral aneurysms by light field particle image velocimetry," in *SPIE Photonics Europe*, pp. 989703–989703, International Society for Optics and Photonics (2016).
- [20] M. D'Angelo, F. V. Pepe, A. Garuccio, and G. Scarcelli, "Correlation Plenoptic Imaging," *Physical Review Letters* **116**, 223602 (2016).
- [21] F. V. Pepe, G. Scarcelli, A. Garuccio, and M. D'Angelo, "Plenoptic imaging with second-order correlations of light," *Quantum Measurements and Quantum Metrology* **3**, 20 (2016).
- [22] F. V. Pepe, F. Di Lena, A. Garuccio, G. Scarcelli, and M. D'Angelo, "Correlation plenoptic imaging with entangled photons," *Technologies* **4**, 17 (2016).
- [23] T. B. Pittman, Y. H. Shih, D. V. Strekalov, and A. V. Sergienko, "Optical imaging by means of two-photon quantum entanglement," *Physical Review A* **52**, R3429 (1995).
- [24] A. Gatti, E. Brambilla, M. Bache, and L. A. Lugiato, "Ghost imaging with thermal light: comparing entanglement and classical correlation," *Physical Review Letters* **93**, 093602 (2004).
- [25] M. D'Angelo and Y. Shih, "Quantum imaging," *Laser Physics Letters* **2**, 567 (2005).
- [26] A. Valencia, G. Scarcelli, M. D'Angelo, and Y. Shih, "Two-photon imaging with thermal light," *Physical Review Letters* **94**, 063601 (2005).
- [27] G. Scarcelli, V. Berardi, and Y. Shih, "Can two-photon correlation of chaotic light be considered as correlation of intensity fluctuations?," *Physical Review Letters* **96**, 063602 (2006).
- [28] J. Mertz, "Introduction to Optical Microscopy", Roberts and Company Publishers (2009).
- [29] M. K. Kim, "Principles and techniques of digital holographic microscopy," *SPIE Reviews* **1**, 018005 (2010).
- [30] M. Hansard, S. Lee, O. Choi, R. Horaud, *Time of Flight Cameras: Principles, Methods, and Applications* (Springer, Berlin Heidelberg, 2013).
- [31] F. Remondino and D. Stoppa (eds.), *TOF Range-Imaging Cameras* (Springer, Berlin Heidelberg, 2013).
- [32] O. Katz, Y. Bromberg, and Y. Silberberg, "Compressive ghost imaging," *Applied Physics Letters* **95**, 131110 (2009).
- [33] M. O. Scully and M. S. Zubairy, *Quantum Optics* (Cambridge University Press, Cambridge, 1997).